PAPER

Hydrodynamic performance of a biomimetic robotic swimmer actuated by ionic polymer–metal composite

Smart Mater. Struct. **22** (2013) 075035 (13pp) doi:10.1088/0964-1726/22/7/075035

Hydrodynamic performance of a biomimetic robotic swimmer actuated by ionic polymer–metal composite

Qi Shen, Tiammiao Wang, Jianhong Liang and Li Wen

Robotic Institute, School of Mechanical Engineering and Automation, Beihang University, Beijing, 100191, People's Republic of China

E-mail: eric.shen1987@gmail.com and alex.wenli@gmail.com

Received 9 November 2012, in final form 4 June 2013
Published 21 June 2013
Online at stacks.iop.org/SMS/22/075035

Abstract
In this paper, we study the thrust performance of a biomimetic robotic swimmer that uses ionic polymer–metal composite (IPMC) as a flexible actuator in viscous and inertial flow, for a comprehensive understanding of IPMC swimmers at different scales. A hydrodynamic model based on the elongated body theory was developed. Based on image analysis, the parameters of the model were identified and simulation results were obtained. To obtain the hydrodynamic thrust performance of the robotic swimmer, we implemented a novel experimental apparatus. Systematic tests were conducted in the servo towing system to measure the self-propelled speed and thrust efficiency under different actuation of IPMC. The undulatory motions of the IPMC swimmer were identified. Experimental results demonstrated that the theoretical model can accurately predict the speed and thrust efficiency of the robotic swimmer. When the Reynolds number of the robotic swimmer was reduced to approximately 0.1%, its speed and thrust efficiency were reduced by 95.22% and 87.33% respectively. It was concluded that the robotic swimmer has a low speed and thrust efficiency when it swims in a viscous flow. Generally, the thrust performance of the robotic swimmer is determined by the kinematics and Reynolds number. In addition, the optimal actuation frequency for the thrust efficiency is greater in a viscous fluid. These results may contribute to a better understanding of the swimming performance of IPMC actuated swimmers in a distinct flow regime (viscous and inertial regime).

(Some figures may appear in colour only in the online journal)

1. Introduction

Ionic polymer–metal composite (IPMC) is one of the promising smart materials for micro biomimetic underwater propulsion [1]. It has the advantage of high flexibility, low drive voltage, and large bending detection. Several pioneering works on IPMC actuated underwater robots have been introduced. The first conceptual design of an underwater robot actuated by ionic polymers was presented by Shahinpoor [2]. Thereafter, some additional biomimetic swimming machines propelled by IPMCs were studied in [3, 4]. A snake-like swimming robot with IPMCs as actuators was designed and experimentally analyzed in [5]. A IPMC-based robotic fish was developed in [6]. A speed model of an IPMC-propelled robotic fish was presented by Tan in [7, 8], which combines the physical-based IPMC model with the classical Lighthill's theory on elongated body. Porfiri developed a modeling framework for predicting the motion of biomimetic underwater vehicles propelled by IPMC [9]. Kim proposed an analytical model of single- or multi-segment IPMC actuators that operate in water [10]. Recently, the wireless actuation and control of IPMC actuators were also investigated [11, 12]. Our previous work proposed an efficiency model of a robotic fish, where the total power consumption of the IPMC was considered in the model [13, 14]. With regard to the size of the IPMC robots, most of the

reported IPMC robots are on a small scale. On the fabrication method, with the advances being made in lithography-based microfabrication, IPMC actuators can be scaled down to the micrometer range to accommodate applications in blood vessels, micro-channels, etc [15–18]. Therefore, the thrust performance of IPMC swimmers on the micro-scale and in viscous fluid (e.g. blood) is important. However, to date, few studies have reported the quantitative thrust performance of IPMC actuated underwater robots on the micro-scale and in viscous fluid.

The first goal of this paper is to study the thrust performance of a robotic swimmer actuated by the IPMC at different scales. Inspired by dolphins, a typical cetacean with amazing swimming skills [19], we developed a biomimetic robotic swimmer propelled by the IPMC. Based on the elongate-body theory of Lighthill [20, 21], a simplified model of the robotic swimmer was developed. Fundamental experiments were conducted. Through image processing, we obtained the parameters of the theoretical model and now present the simulation results.

An important dimensional parameter of swimmers is the Reynolds number *Re*, which is defined as

$$Re = UL/v \tag{1}$$

where L denotes the fish length, U represents the steady swimming speed under the freely swimming condition, and v denotes the kinematic viscosity of the fluid. The Reynolds number of the robotic swimmer is low when its size is reduced (i.e., the length L of the swimmer is small). To experimentally study the robotic swimmer's thrust performance on the micro-scale, one could reduce the Reynolds number by increasing the kinematic viscosity of the fluid. Furthermore, when it is applied to the biomedical device, the aquatic environment where the IPMC operates is viscous. Therefore, hydrodynamic experiments were conducted in viscous and inertial flow.

The thrust efficiency describes a relationship between three parameters: the swimming speed, the time-averaged thrust force, and the time-averaged undulatory power consumed by the fluid. We would measure the three parameters separately. Firstly, the robot swam freely in the fluids, and the speed was measured through image recognition. It was found that the IPMC swimmer at the normal size was able to move in a very viscous flow ($Re \approx 1$). Secondly, experimental apparatus was implemented for obtaining the thrust force of the robotic swimmer under the self-propulsive condition. Thirdly, we estimated the power consumption in the fluid by subtracting the power consumption of the IPMC tail in fluid from that in air. Finally, the experimental results of thrust efficiency were obtained. The theoretical results were compared with the experimental results to verify the model.

Another goal of this paper is to investigate the fish undulatory motion of the IPMC actuated robotic swimmer at different scale. Fish species that primarily use body/caudal fin (BCF) undulation for propulsion, such as eels, tuna and mackerel, display diverse sizes, shapes and kinematics [22]. Eels, mackerel and tuna, termed anguilliform, carangiform and thunniform swimmers, respectively, are the three most typical types of BCF species, and significantly differ in both kinematics and hydrodynamics. Based on previous biological studies, one major criterion that distinguishes the three kinematics is the wavelength of the body during steady swimming [23]. The Reynolds number is one of the important parameters to compare the thrust performance between fish. Many works have reported the efficient swimming of BCF fish for different motion modes (e.g., anguilliform, carangiform and thunniform kinematics) for different Reynolds number [24–26]. Based on the theoretical and experimental results, one could achieve the BCF undulatory motion modes and the corresponding thrust performance. Appropriate kinematics could be chosen for better swimming performance in the distinct flow regime (viscous and inertial flow regime).

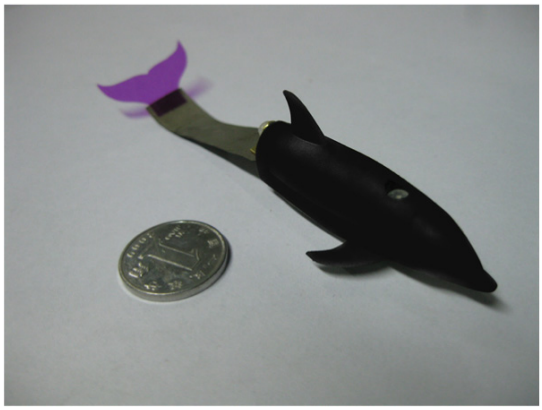

Figure 1. Prototype of the robotic swimmer.

The rest of this paper is organized as follows. The robotic swimmer is described in section 2. The hydrodynamic model is presented in section 3. The parameters are identified in section 4 through fundamental experiments. The experimental investigation on the thrust performance is proposed in section 5. A discussion based on the results is presented in section 6. Section 7 is left for the conclusion.

2. Robotic swimmer prototype development

This section provides a brief introduction to robotic swimmer development. As shown in figure 1, the robotic swimmer prototype consists of three parts: (1) the rigid body shell that acts as the body, (2) the IPMC stripe that acts as the muscle and (3) the plastic piece which mimics the tail fin. The body shell was designed according to the streamlined body proportion of bottlenose dolphins (*Tursiops truncatus*) in Solidworks, whose body shape parameters have been provided in [19, 27]. It was fabricated with nylon plastics using a 3D printer and covered with black matt resin varnish, to thus obtain a smooth surface. The IPMC was attached to the body by two small rectangular conductive copper plates that acted as a clamp. A flexible fin was attached to the end of the IPMC, which was designed based on the shape of a natural dolphin fin (the sweep angle is 35°and the aspect ratio is 3.7).

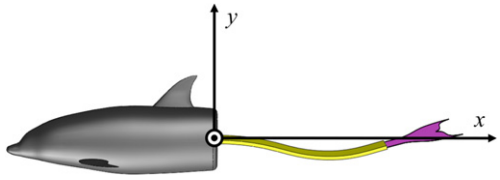

Figure 2. Schematic of the robotic swimmer.

Two wires (Calmont Wire & Cable Inc., USA) were connected to the robot to supply electrical energy to the IPMC actuator. The wires were flexible to avoid interference to the robot during the free swimming process. A counterweight was put in the bottom of the swimmer to achieve buoyancy and enhance the stability of the roll and pitch directions. The robotic swimmer propelled itself by up-and-down motion. It has a total length of 47.5 mm without the tail, 14.5 mm in height and 12 mm at its widest point. Its total weight approximates 5.05 g.

3. Kinematic and dynamic modeling of the robotic swimmer

The main purpose of this section is to develop a simple model for the estimation of the speed and thrust efficiency. In the following subsections, the undulatory motion model of the BCF fish is first introduced and utilized to describe the kinematics of the robotic swimmer [20, 21]. Then we analyzed the rigid head force. Based on Lighthill's elongated body theory (EBT), the speed model and thrust efficiency model of the IPMC-propelled robotic swimmer were obtained.

3.1. Kinematics modeling

The robotic swimmer, whose cross section gradually varies along its length and changes slowly, can be applied with the EBT. We use the BCF fish undulatory motion model to analyze the kinematics of IPMC swimmers. The kinematic movements for all typical BCF swimmers, as approximately fitted from the observed results of a live swimmer [20, 21], can be expressed as

$$h(x, t) = (C_1 x + C_2 x^2)\sin(\omega t + kx) \tag{2}$$

where $h(x, t)$ denotes the displacement of pitch motion, in a body-fixed coordinate system with x measured starting from the clamped end of the IPMC beam, as shown in figure 2. $k = 2\pi/\lambda$ is the wavenumber, corresponding to wavelength λ. While $\omega = 2\pi f$ denotes the circular frequency of oscillation, f represents the flapping frequency, t is the time, and C_1, C_2 can be adjusted to achieve specific values for the amplitude envelope for the entire body.

3.2. Rigid head force modeling

The total force acting on the anterior rigid head of the robotic swimmer takes the following form:

$$F_h = F_{sh} + F_{fh} + F_{ah}, \tag{3}$$

where F_h denotes the total drag force of the rigid head, F_{sh}, F_{fh} and F_{ah} denotes the skin force, the form force and the reactive force of the rigid head, respectively. The form force can be expressed as [28]

$$F_{fh} = 0.5\rho U^2 C_{fh} A_h. \tag{4}$$

A_h denotes the projected area at the cross-section plane, ρ is the fluid density, C_{fh} denotes the form force coefficient, which is expressed as [29]

$$C_{fh} = \frac{6}{1 + \sqrt{Re_h}} + 0.4. \tag{5}$$

The value of Re_h is calculated by $Re_h = L_h U/v$, where L_h denotes the length of rigid head. The skin force of the rigid head can be calculated by the following

$$F_{sh} = 0.5\rho C_{sh} S_h U. \tag{6}$$

S_h denotes the wetted surface area of the rigid head, the skin force coefficient C_{sh} is defined as

$$C_{sh} = 0.059|Re_h^{0.2}|. \tag{7}$$

Given the relatively low value for the added mass coefficient of the swimmer head and the low accelerations during robotic swimmer steady swimming, we assume a negligible reactive force acting on the rigid head, i.e. $F_{ah} = 0$.

3.3. Speed and thrust efficiency modeling

The hydrodynamic model developed by Lighthill is used for capturing the hydrodynamic force produced by the slender body swimmer. The instantaneous thrust $T(t)$ can be expressed as

$$T(t) = \frac{1}{2}\rho A\left[\left(\frac{\partial h}{\partial t}\right)^2 - U^2\left(\frac{\partial h}{\partial x}\right)^2\right]_{x=L_t} - \frac{\mathrm{d}}{\mathrm{d}t}\int_0^{L_t} \rho A\left[\frac{\partial h}{\partial t}\frac{\partial h}{\partial x} + U\left(\frac{\partial h}{\partial x}\right)^2\right]\mathrm{d}x \tag{8}$$

with

$$A = \frac{1}{4\pi S_c^2 \beta}$$

where $x = L_t$ denotes the end of tail, m is the virtual mass density at $x = L_t$, S_c is the width of the tail at $x = L_t$, and β is a non-dimensional parameter close to 1. From the fluid point of view, the swimming speed U in a forward direction is determined by the external force exerted on the swimmer body. The lateral and rotational movements are not obvious when swimming forward. Currently, we only consider the forward direction of the swimmer swimming with lateral and rotational direction constraints. This simplified method has been widely employed in previous experimental and numerical hydrodynamic research [30, 31]. We do not consider complicated physical factors such as the body–caudal fin interaction [32]. The force balance condition in the forward direction can be described as

$$T(t) - F_h = m\frac{\partial U}{\partial t}. \tag{9}$$

Table 1. Dimensions of IPMC beams.

Item	H_I (μm)	L_I (mm)	W_I (mm)
IPMC 1 (tail 1)	200	40	10
IPMC 2 (tail 2)	200	42.5	12

The swimming speed U of the IPMC swimmer can be obtained by solving (9). The Froude efficiency η based on Lighthill's elongate-body theory for steady swimming is employed for the current estimate of thrust efficiency and is given as

$$\eta_{\text{sim}} = \tfrac{1}{2}(1+\delta) \tag{10}$$

with

$$\delta = U/V_b$$

where δ denotes the slip velocity, defined as the ratio of the steady swimming speed U to the body wave speed V_b, and $V_b = \lambda f$.

4. Parameter identification

In this section, we identified the kinematics of the IPMC swimmer in fluids. Two IPMC stripes, manufactured by Environmental Robots Inc., were utilized in the experiments. The dimensions of the IPMC beams are shown in table 1, where W_I, H_I, L_I are the width, thickness and length respectively. We seriously considered and chose the dimensions of our IPMC beams. First, the size of the current IPMC samples are not very different with previous samples that were used for actuating underwater objects [3–9]. In addition, from the visual point of view, the sizes of the IPMCs look appropriate for the size of the rigid fish body. Further, according to our tests, the IPMC actuators have the capability of propelling the whole swimmer.

Besides the above, the focus of this study stems from varying the viscosity of the fluid environment to match up the Reynolds number. This approach allows us to hydro-dynamically investigate the robot swimming at different scales without changing the IPMCs' (and also the fish body's) physical dimensions. Figure 3 shows the experimental setup for the image processing. The IPMC beam was fixed at one end and submerged in the fluids. A signal generator (YX1620P, Yangzhong Pioneer Electronics Co., China) with a power amplifier provided the IPMC actuator with sinusoidal signals. To increase the viscosity of the fluid, we added the glycerin to the water. In this paper, we conducted hydrodynamic experiments in fluids of different viscosities, respectively: 1×10^{-6} m^2 s^{-1} (pure water), 52.1×10^{-6} m^2 s^{-1} (Vis.1), 108.2×10^{-6} m^2 s^{-1} (Vis.2), 163.2×10^{-6} m^2 s^{-1} (Vis.3) and 234.2×10^{-6} m^2 s^{-1} (Vis.4), which were measured by viscometers. The IPMC tail was under voltage amplitude A_v at 2, 2.5, 3 V and actuation frequencies f ranging from 0.4 to 2.4 Hz in water, and at 2.5 V and 0.4–1.8 Hz in viscous fluids ($v > 1 \times 10^{-6}$ m^2 s^{-1}). A camera (HD-3000, Microsoft Inc., USA) was set on the top of the tails for the image acquisition. Images

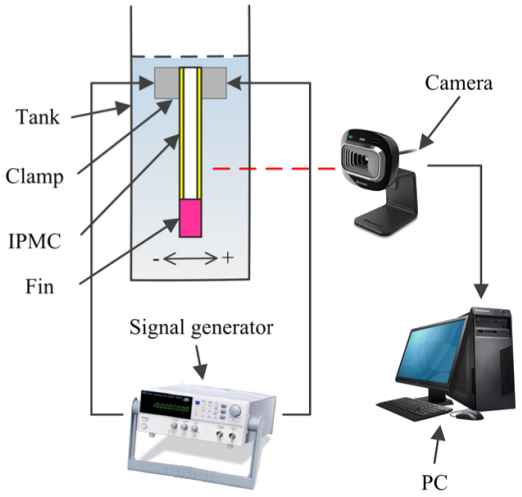

Figure 3. The experimental set up for image capturing.

were captured at 30 frames s^{-1} for approximately 20 s. To identify the parameters of the model, the image analysis of the captured frames was performed in a PC using Matlab (www.mathworks.com/). As indicated by Tsiakmakis, compared with the laser-positioning system, where the measurement of the displacement is only at one point of the actuator and in one direction, the vision based measurement is a total measurement approach that takes into account the whole movement of the actuator [33]. The edge detection algorithm was applied for the image recognition [34]. The angle and magnitude of each point was compared and the points were kept in the same order as their position on the actuators. Then the time track of the IPMC movement was obtained. Through least-square error analysis of the experimental data, the parameters for (2) were derived. Stable oscillating movements of the IPMC tails were observed during the experiments. The cycles were repeated six times under each condition, and the results were obtained by the average. Figure 4 shows that the simulation results of actuation model match well with the real IPMC movement.

The swimming performance of the simulation results is shown. Figure 5 presents two simulation runs, which show the velocity components of the center of mass for two distinct swimming results in the forward direction over 40 s in water. The voltage amplitude A_v was 2.5 V. As can be seen in the graph, after several cycles of undulating movement, the quasi-steady state appears to have been reached.

As indicated by Dewar, the propulsive wavelength is an important kinematic variable involved in the thrust performance, which defines the swimming mode [35]. For the kinematic movement, the wavelength is $\lambda = 0.65L$ for an anguilliform swimmer [36], $\lambda = 0.95L$ for a carangiform swimmer [25], and $\lambda = 1.25L$ for a thunniform swimmer [35]. Figure 6 shows the non-dimensional wavelength of the robotic swimmer. The oscillations of the tails were stable, so the standard deviation of the wavelength approaches zero. The error bars are not shown. It was found that for different voltage amplitudes, the wavelength shows an overall decrease as the actuation frequency increases. It is interesting that

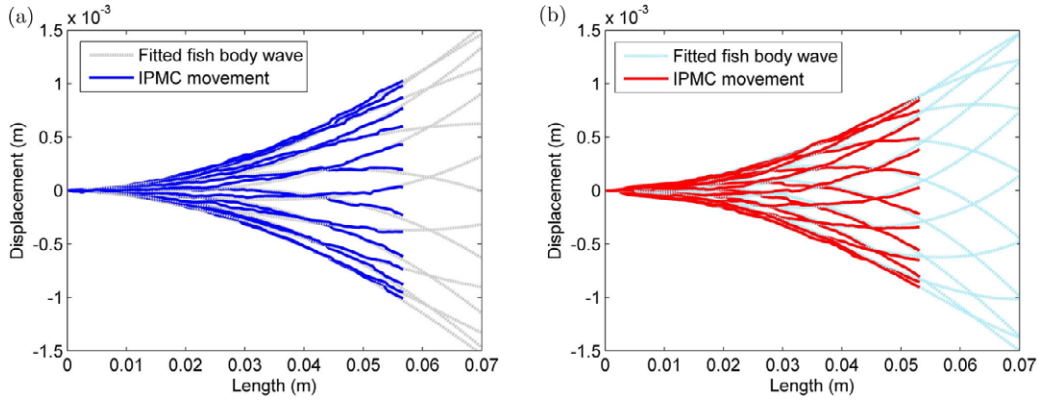

Figure 4. Comparison between the IPMC movement and the fitted fish-body wave in water: (a) tail 1 at the voltage amplitude of 2.5 V and frequency of 1 Hz; (b) tail 2 at 2 V and 1 Hz.

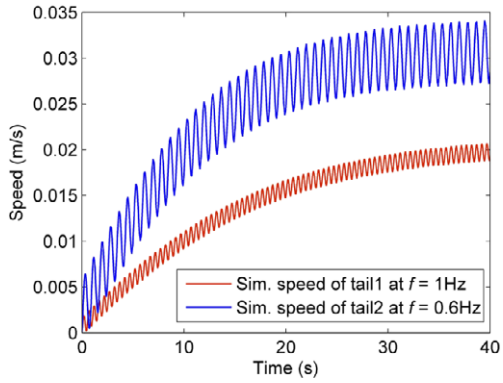

Figure 5. Simulation speed of different tails at an amplitude of 2.5 V in water.

the IPMC actuated swimmer has a thunniform type motion when the actuation frequency was relatively low, has an anguilliform type motion at relatively high frequency, and has a carangiform type between them. As shown in figures 6(a) and (b), the actuation frequency of the IPMC swimmer in water for the thunniform type approximates as 1.4 Hz, for the carangiform type approximates as 2 Hz, and for the anguilliform type approximates as 2.4 Hz. Based on figures 6(c) and (d), the wavelength decreases as the viscosity increases. In a fluid viscosity of 234.2×10^{-6} m^2 s^{-1}, the actuation frequency of the IPMC swimmer for the thunniform type approximates as 0.6 Hz, for the carangiform type approximates as 1.2 Hz, and for the anguilliform type approximates as 1.6 Hz.

5. Experimental investigation and results

In this section, we experimentally studied the thrust performance of the robotic swimmer. First, the experimental apparatus will be introduced in section 5.1. The expression of the thrust efficiency can be presented as

$$\eta_{\text{exp}} = \frac{U_{\text{exp}} T_{\text{exp}}}{P_{\text{exp}}}. \tag{11}$$

Then the experimental data of speed U_{exp}, thrust T_{exp} and power consumption P_{exp} are measured separately in sections 5.2, 5.3 and 5.4. Finally, the experimental results of the thrust efficiency are obtained in section 5.5.

5.1. General experimental set up

First, we introduce the experimental method. A horizontal low-velocity servo towing system with force detection apparatus was implemented. This servo towing system has been utilized previously for the purpose of obtaining quantitative hydrodynamics of a self-propulsion underwater robot [37–40]. The water tunnel has a running speed ranging from 0.005 to 1 m s^{-1}, and the uniformity of the flow velocity is 0.2%.

Figure 7 shows the mechanical components of the self-propelled experimental apparatus, where the robotic swimmer and its affiliated components are fixed vertically under two component force transducers (CFBLSM, BGTSE Inc., China) which are attached to the carriage by screws. The force transducer has a measuring range of 1 N and a sensitivity of 0.01 N in the axial direction. The robotic swimmer is submerged under the fluid through a carbon fiber shaft, while its transmission mechanism is mounted on a metal plate and is above the surface of the fluid. The force T_1, T_2 (see figure 7) is measured by the force transducers. A low-resistance bearing is set at the joint. According to the lever principle, the resultant force on the swimmer is amplified by 100 times when it is transferred to the force sensor. Thus, the external force T_{ext} from the external apparatus acting on the swimmer could be measured by $T_{\text{ext}} = (T_1 - T_2)/100$. The center of mass G of the swimmer is set right under the shaft to minimize the influence of gravity during the experiments.

The water tank, with the size of 7.8 m × 1.2 m × 1.1 m, is filled with a mixture of water and glycerin. The robotic swimmer, located at the mid-depth in the tank, has sufficient space in the tank to move without being affected by the free surface, boundaries on both sides and bottom of the tank. A data recorder (Nicolet Vision XP, LDS Inc., Germany) was used to record the experimental results, which has 16 sampling channels and a maximum sampling rate of 100 kHz.

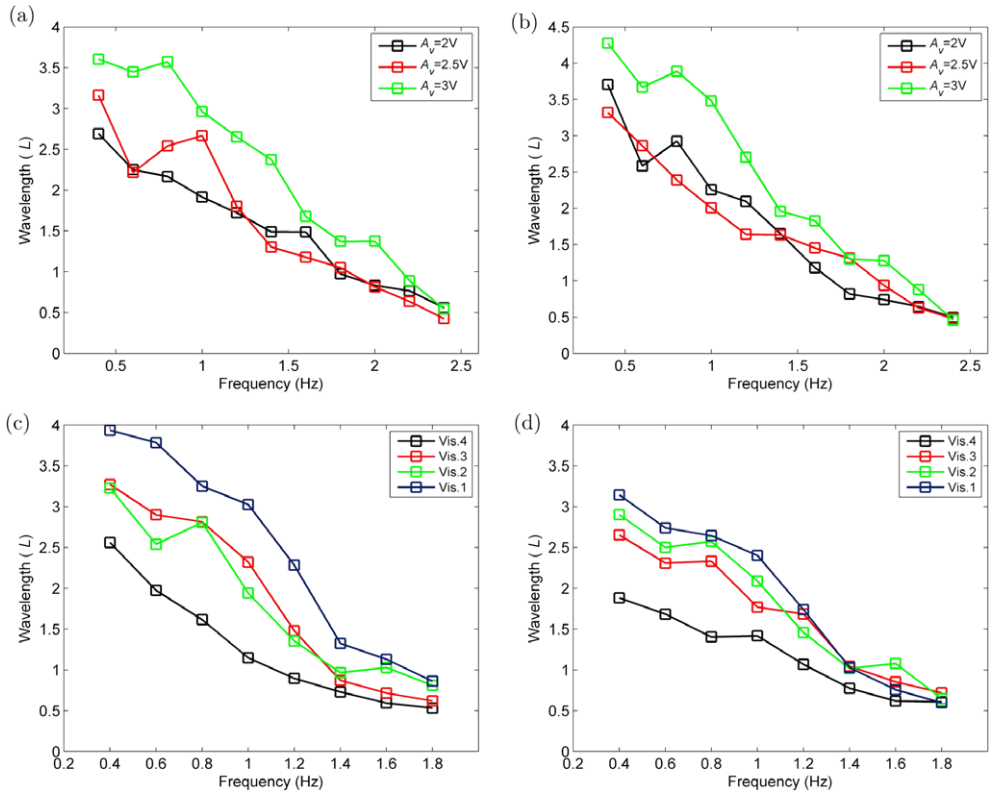

Figure 6. Experimental results of the wavelength (the results were averaged from six cycles under each condition): (a) tail 1 in water (the viscosity is 1×10^{-6} m^2 s^{-1}); (b) tail 2 in water (the viscosity is 1×10^{-6} m^2 s^{-1}); (c) tail 1 in viscous fluids ($A_v = 2.5$ V); (d) tail 2 in viscous fluids ($A_v = 2.5$ V).

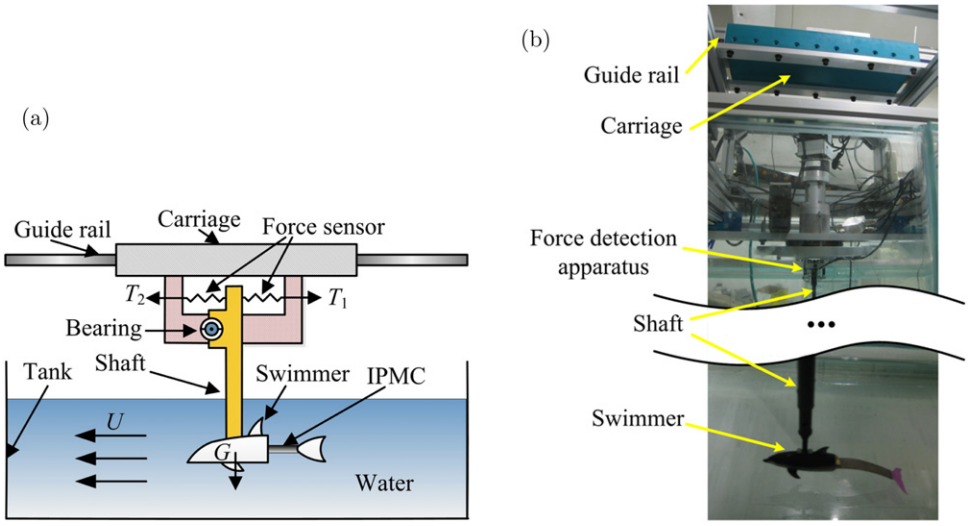

Figure 7. Experimental set up: (a) illustration of experimental apparatus; (b) snapshot of the thrust measurement system.

5.2. Experiment 1: speed

In this subsection, the speed of the robotic swimmer was tested. In this experiment, the robotic swimmer propelled by the IPMC tail swam freely in a tank, and its motion was recorded by the camera. The velocities were measured through the algorithm. Under each condition, the robot swimming performance was repeated three times and the experimental results of the cruising speed were obtained from the average. Figure 8 shows consecutive snapshots of the swimmer swimming in the tank.

Based on the experimental results, we validated the capability of the model in predicting the cruising speed of the robotic swimmer. Figure 9 shows the comparison between the simulation results and the experimental results of the speed. It can be found that the IPMC swimmer at normal size was able

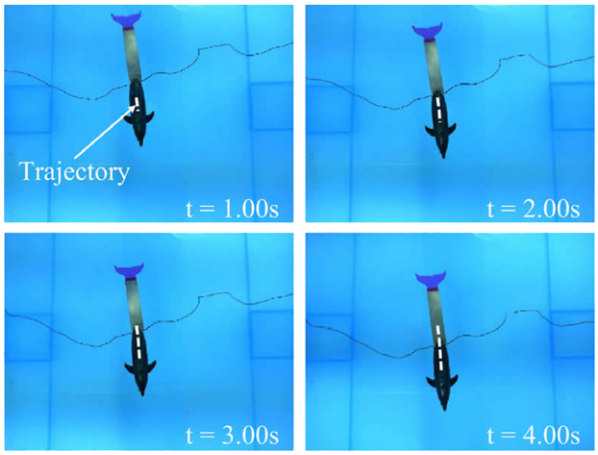

Figure 8. Consecutive snapshots of the robotic swimmer in water.

to move in very viscous flow. The predicted speed matches the experimental data well. In water, there is an optimal frequency that approximates 1 Hz under which the swimmer reaches the highest speed. As shown in figures 9(a) and (b), with the voltage amplitude increasing, the speed of the IPMC swimmer increases. By comparing the experimental results of tail 1 and tail 2, one can find that the velocities of tail 2 are generally higher than that of tail 1. This means that the speed can be improved by increasing the voltage amplitude as well as the size of the IPMC. It should be noted that as the viscosity rises, its velocity has a significant decrease, and when the viscosity increases, the optimal frequency for the speed increases, which is shown in figures 9(c) and (d). For instance, at a fluid viscosity of 1×10^{-6} m^2 s^{-1} and a voltage amplitude of 2.5 V, the highest velocity for tail 1 was 2.27×10^{-2} m s^{-1}, recorded at a frequency of 0.8 Hz and the Reynolds number was 2.27×10^3. While at 234.2×10^{-6} m^2 s^{-1} and 2.5 V, the highest velocity for tail 1 was 2.45×10^{-3} m s^{-1}, recorded at 1.2 Hz and the Reynolds number was 1. The Reynolds number decreases to 0.1%, which means that the scale of the IPMC swimmer decreases to approximately 0.1%. The results show that the robotic swimmer has a low speed at the micro-scale ($Re \approx 1$).

5.3. *Experiment 2: thrust force*

In this subsection, we studied the thrust force of the IPMC swimmer through hydrodynamic experiments. The thrust and drag of the robotic swimmer are combined together during the swimming process, so the thrust force cannot be measured directly. It should be noted that in most conventional dragging hydrodynamic experimental methods of robotic model, the force $T_{\text{ext}} \neq 0$ along the forward direction, which means the thrust force was not equal to the drag force [41–45]. As a result, the external force was absorbed by the external apparatus. Thus the robotic fish was not self-propelled and

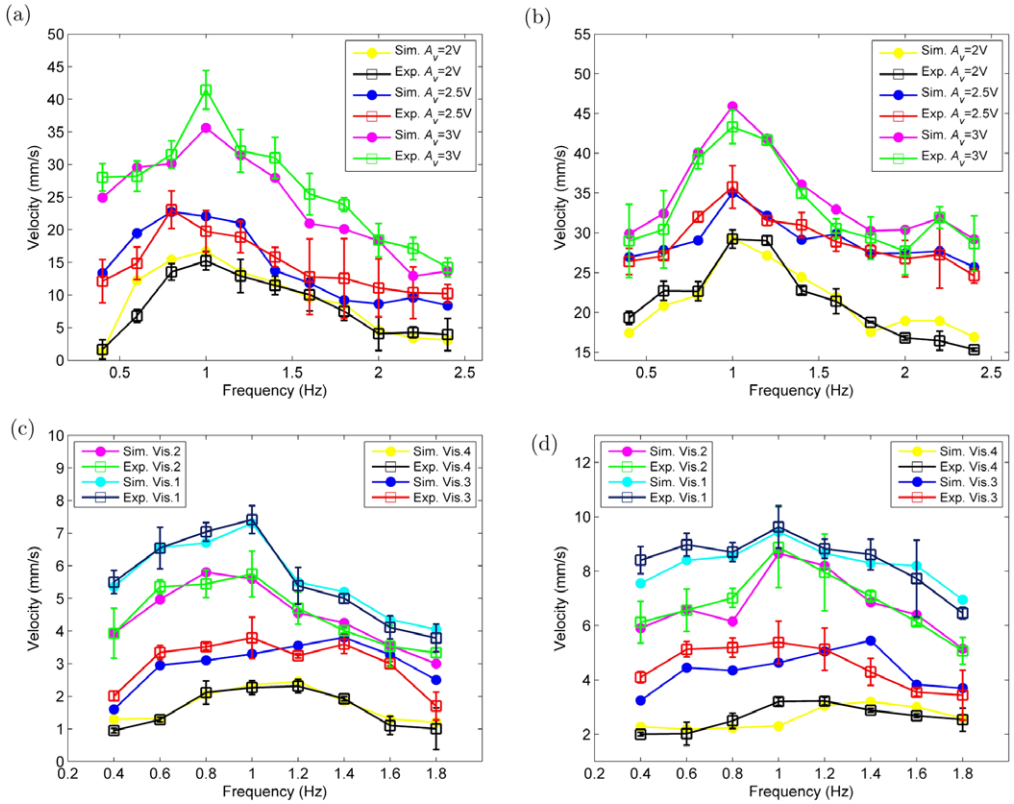

Figure 9. Speed comparison between simulation results and experimental results (the results were averaged from three trials under each condition): (a) tail 1 in water (the viscosity is 1×10^{-6} m^2 s^{-1}); (b) tail 2 in water (the viscosity is 1×10^{-6} m^2 s^{-1}); (c) tail 1 in viscous fluids ($A_v = 2.5$ V); (d) tail 2 in viscous fluids ($A_v = 2.5$ V).

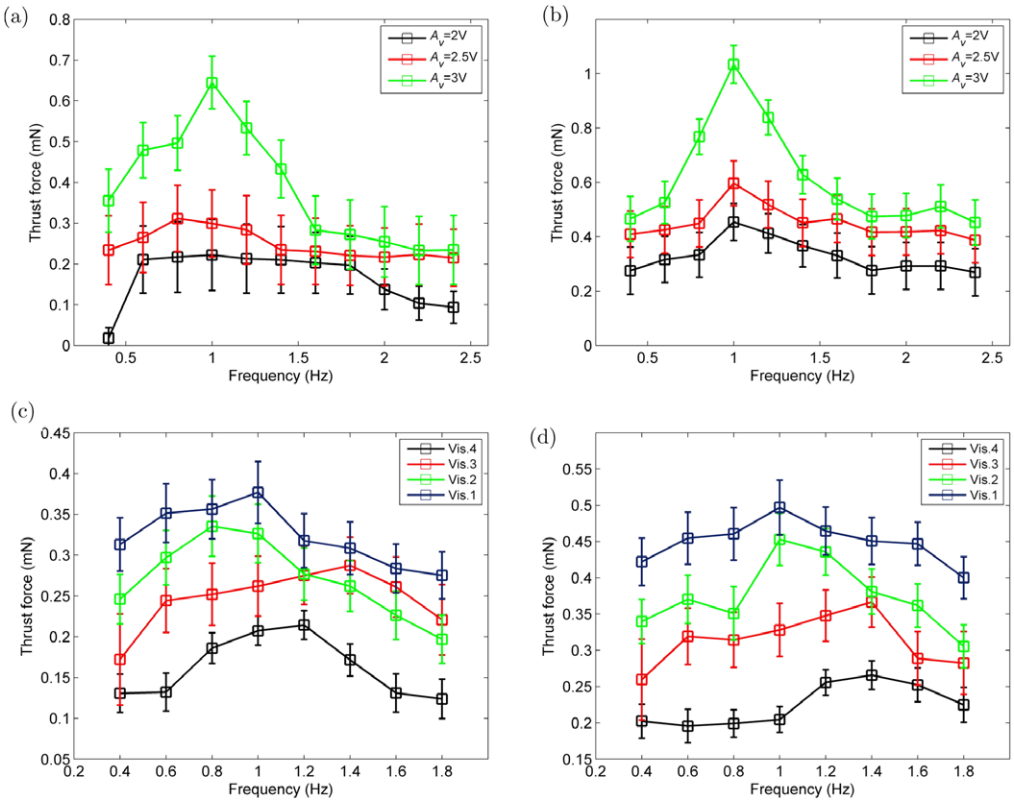

Figure 10. Experimental results of thrust force (the results were averaged from three trials under each condition): (a) tail 1 in water (the viscosity is 1×10^{-6} m^2 s^{-1}); (b) tail 2 in water (the viscosity is 1×10^{-6} m^2 s^{-1}); (c) tail 1 in viscous fluids ($A_v = 2.5$ V); (d) tail 2 in viscous fluids ($A_v = 2.5$ V).

there was no equality between the thrust and drag force. Taking both the active and passive towing approaches into consideration, a novel experimental approach was proposed.

Firstly, the swimmer was towed under the servo towing system at its cruising speed U_{exp} with corresponding sinusoidal wave voltage input. During the drag experiment, we adjusted the towing speed to ensure the external force $T_{ext} = 0$. Thus we can avoid the interference of the wires under the freely swimming condition. According to Newton's law, the robotic swimmer was considered to swim freely without the external force from the apparatus above acting on it when the detected force $T_{ext} = (F_D - T_{exp}) \times 100 = 0$, where the drag force F_D equaled to the thrust force T_{exp}. Secondly, the swimmer was towed without input voltage, and the force detection apparatus measured F_D. Finally, T_{exp} was obtained since $T_{exp} = F_D$ under the self-propelled condition. In this paper, the drag experiments were repeated three times under each condition. For the details of the experimental thrust force measurement method please refer to our previous study on the IPMC fish [13, 14].

Figure 10 shows the experimental thrust force of the robotic swimmer produced by different tails. At low viscosity, the tails produces the highest thrust force when the frequency approximates 1 Hz, which had a good agreement with the speed data in figure 9. The optimal frequency for the thrust force increases with increasing viscosity. It was also found that with the viscosity of the fluid increasing, the thrust force decreases.

5.4. Experiment 3: power consumption

To obtain the power output of the robotic swimmer in fluids, we need to test the oscillation of the IPMC tail under different circumstances. The equivalent beam model for IPMC actuators developed by Kim was utilized to estimate the power consumption [46]. The blocking force, F_b, of a cantilevered IPMC actuator can be written as follows:

$$F_b = \frac{3W_I H_I E d}{8L_I} V \tag{12}$$

with

$$d = \frac{2s_a H_I^2}{3L_I^2 V}$$

where V is the input voltage, s_a is the deflection of the IPMC in air and E is the Young's modulus. The amplitude of the tail is far smaller than its length scale, so the tail is supposed to bend periodically at the tip. The IPMC tail oscillated in air and the tip displacement s_a was measured through image processing. Then, the IPMC tail oscillated in fluid under the same input condition and we measured the oscillation s_f. It was found that under the same condition, the deflection of the IPMC tail in air operation is larger than that in water operation, which was discussed in [47]. Since the passive fin attached to the IPMC beam was very light and flexible compared to the IPMC, its equivalent beam dynamics was ignored in the analysis here. By subtracting the power

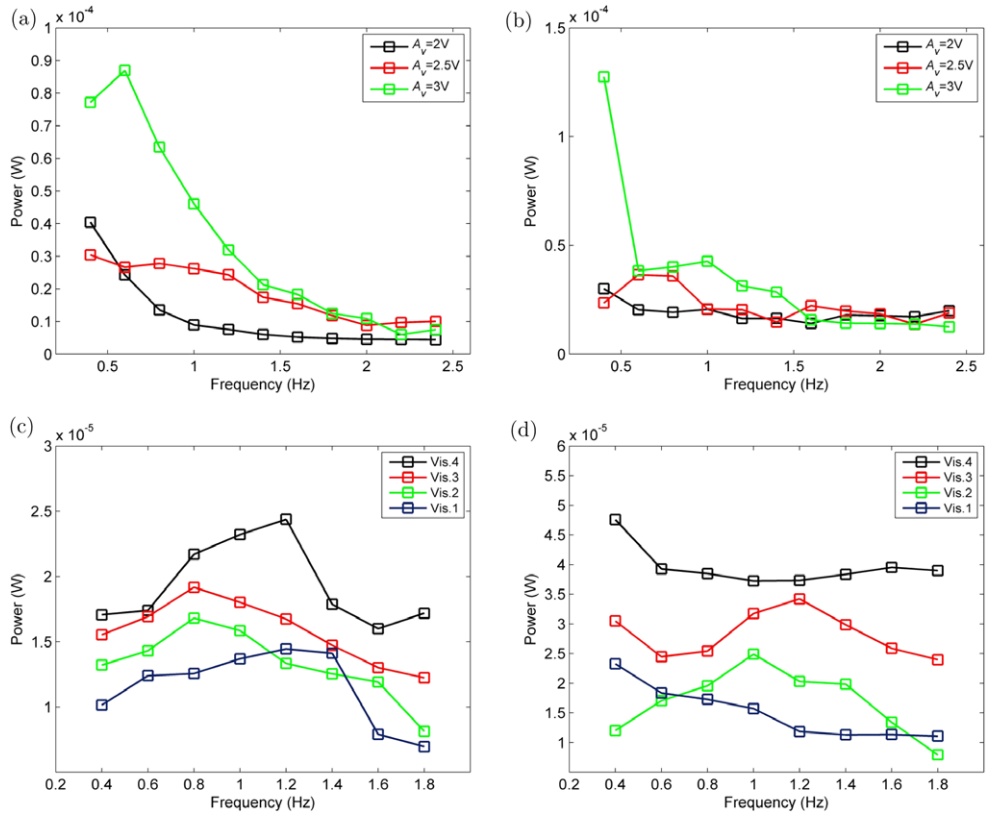

Figure 11. Experimental results of power consumption (the results were averaged from six cycles under each condition): (a) tail 1 in water (the viscosity is 1×10^{-6} m^2 s^{-1}); (b) tail 2 in water (the viscosity is 1×10^{-6} m^2 s^{-1}); (c) tail 1 in viscous fluids ($A_v = 2.5$ V); (d) tail 2 in viscous fluids ($A_v = 2.5$ V).

consumption of the IPMC in fluid P_f from that in air P_a, the average power that the IPMC output in the fluid during one cycle at frequency f can be obtained as:

$$P_{exp} = P_a - P_f = \frac{\int_{t_s}^{1/f+t_s} F_b \, ds_a - \int_{t_s}^{1/f+t_s} F_b \, ds_f}{1/f}$$
$$= \frac{fW_I H_I^3 E \int_{t_s}^{1/f+t_s} s_a (ds_a - ds_f)}{4L_I^3}, \quad (13)$$

where t_s is a random time point during the IPMC tail performance. The cycles of the IPMC tail oscillating movements were repeated six times under each condition, and the results were obtained by the average. Figure 11 gives the power output of the two IPMC tails in the fluids. Little difference was noticed between the cycles due to the stability of the oscillations. The standard deviation of the power consumption approaches zero, and the error bars are not shown. From figures 11(a) and (b), it can be seen that with increasing operating frequency, the power output in the fluid of the IPMC tail decreases, and the power output can be increased by increasing the voltage. It is also noticed that as the viscosity of the fluid increases, the displacement of the IPMC tail has a significant decrease and the power output shows an overall rise, as shown in figures 11(c) and (d).

5.5. Experimental results of thrust efficiency

Finally, we derived the experimental thrust efficiency of the IPMC swimmer. Based on the measured thrust force T_{exp}, speed U_{exp}, power consumption P_{exp} and with (11), the experimental data of the thrust efficiency η_{exp} was obtained.

The capability of the thrust efficiency model (see (10)) in predicting the efficiency was verified for different voltages, operating frequencies and fluid viscosities. Figure 12 shows that the proposed model can accurately predict the thrust efficiency. Based on figures 12(a) and (b), it can be observed that initially, the efficiency increases as the frequency increases. Its thrust efficiency reaches the maximum when the frequency is approximately 1 Hz. With the frequency being relatively high, the efficiency decreases. It was also noticed that the IPMC swimmer at high input voltage has a relatively high thrust efficiency.

The thrust efficiency of the IPMC swimmer varies with different tails, and each tail has its optimal frequency for the thrust efficiency. Generally, the thrust efficiency of tail 2 is higher than that of tail 1. Thus it was demonstrated that by increasing the input voltage as well as the size of the IPMC, the thrust efficiency of the robotic swimmer can be improved. It was also found that with the viscosity increasing, the Reynolds number and the thrust efficiency of the robotic swimmer decreases. At a fluid viscosity of 1×10^{-6} m^2 s^{-1} and a voltage amplitude of 2.5 V, the peak thrust efficiency for tail 2 was 53.36%, recorded at an actuation frequency of 1 Hz and the Reynolds number was 3.5×10^3. While at 234.2×10^{-6} m^2 s^{-1} and 2.5 V, the peak thrust efficiency for tail 2 was 6.76%, recorded at 1.4 Hz and the Reynolds number was 1.37. The Reynolds number decreases to approximately

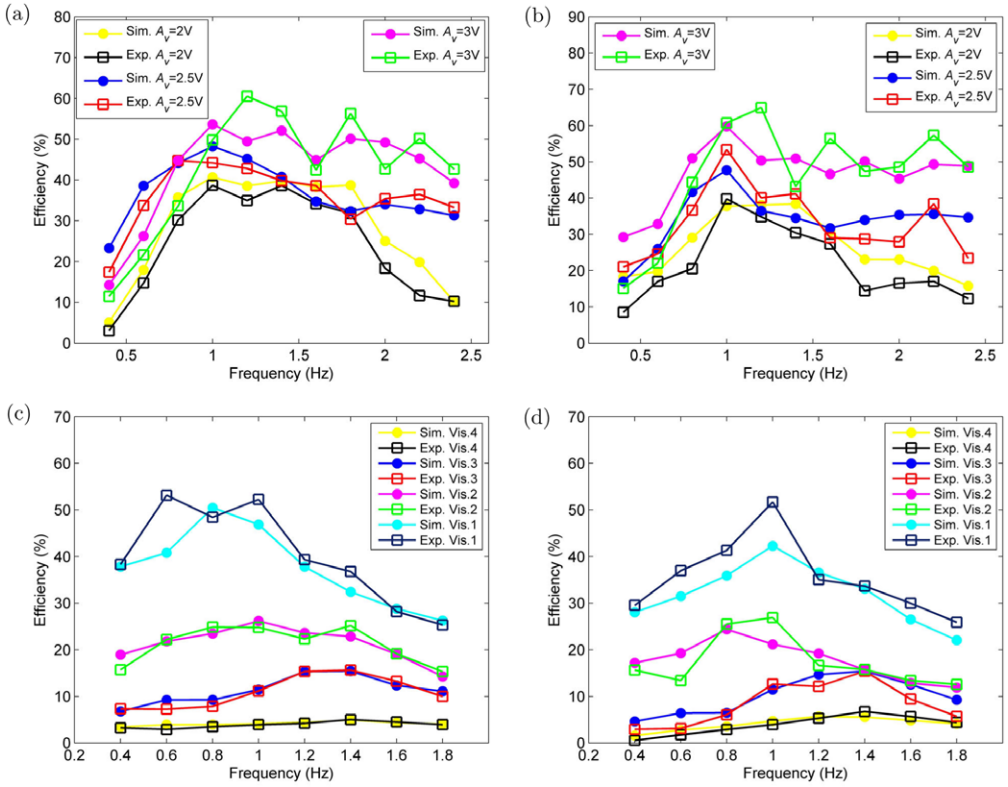

Figure 12. Thrust efficiency comparison between simulation results and experimental results: (a) tail 1 in water (the viscosity is 1×10^{-6} m^2 s^{-1}); (b) tail 2 in water (the viscosity is 1×10^{-6} m^2 s^{-1}); (c) tail 1 in viscous fluids ($A_v = 2.5$ V); (d) tail 2 in viscous fluids ($A_v = 2.5$ V).

0.1%, which means the scale of the IPMC swimmer is reduced to 0.1%. One could indicate that the thrust efficiency of the robotic swimmer decreases when its scale is reduced. As the viscosity increases, the optimal frequency for the thrust efficiency increases, as shown in figures 12(c) and (d).

6. Discussion

6.1. Thrust performance of an IPMC actuated underwater robot at different scale

IPMC actuators have various promising applications in swimming structures, biomimetic robots, bio/micromanipulation and biomedical devices [2–6]. To the best of our knowledge, there have been very limited works done on the hydrodynamic performance of IPMC-propelled swimmers at the micro-scale. In this paper, we theoretically and experimentally studied the thrust performance of a biomimetic robotic swimmer, for a comprehensive understanding of IPMC swimmers at different scales. We found that the IPMC swimmer at normal size was able to move in very viscous flows ($Re \approx 1$). A novel experimental apparatus was implemented to obtain the bio-kinematic parameters and the thrust performance of IPMC swimmers. The self-propelled speed and thrust efficiency were measured under the system. Encouraged by the potential generality of this measurement method, we believe that the servo towing system and the self-propelled approach also offers a platform to experimentally study the thrust efficiency of underwater robots actuated by other types of smart materials.

Present experimental results can be useful for better thrust performance control of IPMC swimmers at different scales. We observed that, in water, the speed and the thrust efficiency of the IPMC swimmer at normal size can be increased by increasing the amplitude of the voltage. The optimal actuation frequencies for the speed and thrust efficiency both approximate to 1 Hz during the steady swimming state. In viscous fluids, (i.e., the size of the IPMC swimmer is scaled down), the speed and thrust efficiency both have an overall decrease compared with that in water. Although the optimal frequency for the speed still approximates as 1 Hz, one needs to increase the actuation frequency (approximates 1.4 Hz at $Re \approx 1$) to achieve a high thrust efficiency at a low Reynolds number. By increasing the size of the IPMC actuator, the speed and thrust efficiency of the IPMC swimmer can also be improved in a distinct flow regime (viscous and inertial regime). The theoretical model and experimental results might possibly shed light on the efficient design and control of the IPMC actuated robotic swimmer: the robotic swimmer could determine the proper movement patterns to achieve a better thrust performance depending on the situation and scale in order to save power, i.e. for missions or requirements that require a high speed or efficient cruising.

6.2. Investing fish biomechanics with IPMC actuated underwater robot

Great efforts have been made to understand fish undulatory propulsion, but the inability to control and precisely alter

Table 2. The thrust efficiency and speed results and comparisons.

Re	Item	Anguilliform	Carangiform	Thunniform
$Re \approx 1$	η_{exp} tail1 (%)	4.5	4.2	3.5
	η_{exp} tail 2 (%)	5.6	5.3	2.9
	U_{exp} tail 1 (10^{-3} m s^{-1})	1.1	2.3	1.3
	U_{exp} tail 2 (10^{-3} m s^{-1})	2.7	3.2	2
$Re \approx 1000$	η_{exp} tail1 (%)	33.2	35.4	39.8
	η_{exp} tail 2 (%)	23.4	27.9	41.2
	U_{exp} tail 1 (10^{-3} m s^{-1})	10.2	11.1	15.8
	U_{exp} tail 2 (10^{-3} m s^{-1})	24.6	26.8	31.0

individual kinematic parameters has hampered biologists' ability to understand the fundamental mechanics of aquatic systems [24]. Smart materials, mechatronics, and related techniques have become increasingly important in experimental biology, offering the opportunity to focus research by creating robotic models that can easily be controlled to move with the desired kinetic mechanisms [48–51]. It should be noted that many robot model developed before used the rigid fish-body mechanism, which cannot accurately imitate the live fish body [41–44]. According to previous work, when compared to a rigid flapping foil, the thrust efficiency of a two-dimensional flapping foil with chord-wise flexibility was experimentally shown to increase significantly, i.e., up to 36% [31]. In our study, IPMC, as the flexible underwater actuator, was applied to the hydrodynamic study of a laboratory robotic swimmer with the self-propelled method for the first time.

The current study is beneficial for better understanding the fish undulatory kinematics with varied body size. Taking into account the thrust efficiency and speed as reported in table 2, it is interesting to note that at low Reynolds number, the thrust efficiency of the robotic swimmer in anguilliform type, i.e., 4.5% for tail 1 and 5.6% for tail 2, is the highest. While the thrust efficiency in thunniform type, 3.5% for tail 1 and 2.9% for tail 2, is the lowest. In contrast, at high Reynolds number, the thrust efficiency of the robotic swimmer in anguilliform type were 33.2% for tail 1, 23.4% for tail 2 and is the lowest. The thrust efficiency in thunniform type is the highest, i.e., 39.8% for tail 1 and 41.2% for tail 2. The value for carangiform kinematics is intermediate between that for anguilliform and thunniform kinematics. From the perspective of speed, at high Reynolds number, the robotic swimmer with thunniform kinematics not only reaches a higher thrust efficiency, but also achieves the maximum velocity among all three kinetic types. The carangiform type wins the race of speed at low Reynolds number in the present experiment. It is also noticed that the thrust efficiency in high Reynolds number is higher than that in low Reynolds number.

From the biological aspect, the presented thrust efficiency shows that during a steady swimming state at large scale, (i.e., at high Reynolds number), thunniform kinematics is the most efficient, while anguilliform kinematics produces a relatively poor thrust efficiency; carangiform kinematics is intermediate between the two. At small scale (i.e., at low Reynolds number), it is the reverse situation: the fish has the highest thrust efficiency with the anguilliform type. It is less efficient with the thunniform type and the carangiform type is between them. Despite the kinematic effect, the thrust efficiency increases as the Reynolds number increases. Furthermore, it can be indicated that as the fish develops from juvenile to adult, increasing the wavelength of the undulatory motion can result in high thrust efficiency and steady swimming speed. Meanwhile, the peak thrust efficiency can also increase as its body size rises. Similar results were observed in the comparison between anguilliform type and carangiform type, which were carried out by Borazjani through numerical investigation [52]. It is also found that the wavelength for the optimal thrust efficiency in water is within the range $2L$–$4L$, which does not approach the range of wavelength that most live swimmers achieve in nature ($0.65L$–$1.25L$). This reflects the efficiency disparity between IPMC swimmers and live swimmers.

7. Conclusion

In this paper, we focused on an IPMC-propelled biomimetic robotic swimmer's thrust performance at different scales. To study the thrust performance at different Reynolds number, the robotic swimmer was tested in the fluids with varied viscosities. According to the experimental apparatus which we developed recently, the self-propelled speed, thrust force and power consumption were measured and the thrust efficiency was obtained. The maximum velocity and thrust efficiency of the robotic swimmer in water were 4.6×10^{-2} m s^{-1} and 66.5%, respectively and the recorded frequencies and voltage amplitude approximated as 1 Hz and 3 V. When the robotic swimmer's scale reduced to 0.1%, the peak speed was 2.2×10^{-3} m s^{-1}, recorded at a frequency of 1.2 Hz and voltage amplitude of 2.5 V, and the peak thrust efficiency was 6.76%, recorded at 1.4 Hz and 2.5 V. Based on the hydrodynamic data of the robotic swimmer, it was concluded that the robotic swimmer has a low speed and thrust efficiency when it is scaled down. The optimal actuation frequency for the speed and thrust efficiency increases as the fluid viscosity rises. It was also noteworthy that the thrust performance can be improved by increasing the size of the IPMC as well as the actuation voltage.

The present method and experimental apparatus also allow us to investigate the fish biomechanics, which cannot be easily tackled experimentally with live fish. We found that the kinematics and Reynolds number have an important influence on the thrust performance of the BCF IPMC swimmer. Some quantitative data to address this issue were

provided. The wavelength of the IPMC swimmer decreases as the actuation frequency increases, and its undulatory motion varies from thunniform type to anguilliform type at relatively high frequencies. It should be noticed that at low Reynolds number ($Re \approx 1$), the thrust efficiency of the swimmer in the anguilliform type is higher than that in the thunniform type. While at high Reynolds number ($Re \approx 1 \times 10^3$), the anguilliform type has a lower thrust efficiency than the thunniform type. This method and the experimental apparatus may also be helpful for studying the thrust performance of other smart material actuated underwater robots at multi-scales.

After millions of years of evolution, fish and ocean mammals are the ultimate examples of superior swimmers, with excellent speed, agility and efficiency [53]. In the future, we will focus on developing an underwater robot actuated by multi-IPMCs, to mimic the kinematics of live BCF swimmers. Based on the hydrodynamic results presented in this paper, efficient swimming control of an IPMC actuated robotic swimmer will be studied in the future.

Acknowledgments

Many thanks to Lei Bao for helping to improve this paper. This work was supported by National Natural Science Foundation of China (No. 61075100). The authors would like to thank the referees for careful reading of the manuscript and for their helpful comments.

References

[1] Bhandari B, Lee G and Ahn S 2012 A review on IPMC material as actuators and sensors: fabrications, characteristics and applications *Int. J. Precis. Eng. Manuf.* **13** 141–63

[2] Shahinpoor M 1992 Conceptual design, kinematics and dynamics of swimming robotic structures using ionic polymeric muscles *Smart Mater. Struct.* **1** 91–4

[3] Chamorro G 2000 Swimming robotic structures equipped with IPMC artificial muscles *MSc Thesis* University of New Mexico

[4] Mojarrad M 2001 Study of ionic polymeric gels as smart materials and artificial muscles for biomimetic swimming robotic applications *PhD Dissertation* University of New Mexico

[5] Yamakita M, Kamamichi N, Kozuki T, Asaka K and Luo Z W 2005 A snake-like swimming robot using IPMC actuator and verification of doping effect *Proc. IEEE/RSJ Int. Conf. on Intelligent Robots and Systems (Edmonton, AB, CA, 2005)* pp 2035–40

[6] Tan X B, Kim D, Usher N, Laboy D, Jackson J, Kapetanovic A, Rapai J, Sabadus B and Zhou X 2006 An autonomous robotic fish for mobile sensing *Proc. IEEE/RSJ Int. Conf. on Intelligent Robots and Systems (Beijing, CHN, 2006)* pp 9–15

[7] Chen Z, Shatara S and Tan X B 2010 Modeling of biomimetic robotic fish propelled by an ionic polymer–metal composite caudal fin *IEEE/ASME Trans. Mechatronics* **15** 448–59

[8] Mbemmo E, Chen Z, Shatara S and Tan X B 2008 Modeling of biomimetic robotic fish propelled by an ionic polymer–metal composite actuator *Proc. IEEE/RSJ Int. Conf. on Robotics and Automation (Pasadena, CA, USA, 2008)* pp 689–94

[9] Aureli M, Kopman V and Porfiri M 2010 Free-locomotion of underwater vehicles actuated by ionic polymer metal composites *IEEE/ASME Trans. Mechatronics* **15** 603–14

[10] Yim W, Lee J and Kim K J 2007 An artificial muscle actuator for biomimetic underwater propulsors *Bioinsp. Biomim.* **2** 31–41

[11] Abdelnour K, Stinchcombe A, Porfiri M, Zhang J and Childress S 2012 Wireless powering of ionic polymer metal composites toward hovering microswimmers *IEEE/ASME Trans. Mechatronics* **17** 924–35

[12] Lee J S, Yim W, Bae C and Kim K J 2012 Wireless actuation and control of ionic polymer–metal composite actuator using a microwave link *Int. J. Smart Nano Mater.* **3** 1–19

[13] Wang T, Shen Q, Wen L and Liang J 2012 On the thrust performance of an ionic polymer–metal composite actuated robotic fish: modeling and experimental investigation *Sci. China Technol. Sci.* **55** 3359–69

[14] Shen Q, Wang T, Wen L, Liang J and Chen Y 2012 On the thrust efficiency of an IPMC actuated robotic swimmer: dynamic modeling and experimental investigation *Proc. Int. Offshore and Polar Engineering Conf. (Rhodes, Greece, 2012)* pp 556–62

[15] Chen Z and Tan X 2010 Monolithic fabrication of ionic polymer-metal composite actuators capable of complex deformation *Sensors Actuators* A **157** 246–57

[16] Zhou J, Chan H, To T, Lai K and Li W 2004 Polymer MEMS actuators for underwater micromanipulation *IEEE/ASME Trans. Mechatronics* **9** 334–42

[17] Feng G and Chen R 2008 Improved cost-effective fabrication of arbitrarily shaped IPMC transducers *J. Micromech. Microeng.* **18** 015016

[18] Cho S M and Lee D W 2009 A biomimetic micro-collector based on an ionic polymer metal composite *Microelectron. Eng.* **86** 916–9

[19] Fish F E 1993 Power output and propulsive efficiency of swimming bottlenose dolphins (tursiops truncatus) *J. Exp. Biol.* **185** 179–93

[20] Lighthill M J 1960 Note on the swimming of slender fish *J. Fluid Mech.* **9** 305–17

[21] Lighthill M J 1970 Aquatic animal propulsion of high hydromechanical efficiency *J. Fluid Mech.* **44** 265–301

[22] Tytell E D 2007 Do trout swim better than eels? Challenges for estimating performance based on the wake of self-propelled bodies *Exp. Fluids* **43** 701–12

[23] Webb P W 1984 Body form, locomotion and foraging in aquatic vertebrates *Integr. Comp. Biol.* **24** 107–20

[24] Lauder G V 2011 Swimming hydrodynamics: ten questions and the technical approaches needed to resolve them *Exp. Fluids* **51** 23–35

[25] Müller U, Heuvel B, Stamhuis E and Videler J 1997 Fish foot prints: morphology and energetics of the wake behind a continuously swimming mullet (Chelon labrosus Risso) *J. Exp. Biol.* **200** 2893–906

[26] Blake R W and Domenici P 2000 *Biomechanics in Animal Behaviour* (Oxford: BIOS Scientific)

[27] Yu J, Hu Y, Fan R, Wang L and Huo J 2006 Construction and control of biomimetic robotic dolphin *Proc. IEEE/RSJ Int. Conf. on Robotics and Automation (Orlando, FL, 2006)* pp 2311–6

[28] Batchelor G K 1967 *An introduction to Fluid Dynamics* (Cambridge: Cambridge University Press)

[29] McHenry M J, Azizi E and Strother J A 2003 The hydrodynamics of locomotion at intermediate Reynolds numbers: undulatory swimming in ascidian larvae (Botrylloides sp.) *J. Exp. Biol.* **206** 327–43

[30] Barrett D, Triantafyllou M, Yue D, Grosenbaugh M and Wolfgang M 1999 Drag reduction in fish-like locomotion *J. Fluid Mech.* **392** 183–212

[31] Prempraneerach P, Hover F and Triantafyllou M 2003 The effect of chordwise flexibility on the thrust and efficiency of a flapping foil *Proc. 13th Int. Symposium on Unmanned Untethered Submersible Technology (Durham, USA,2003)* pp 120–8

[32] Wolfgang M J, Anderson J M, Grosenbaugh M A, Yue D K and Triantafyllou M S 1999 Near-body flow dynamics in swimming fish *J. Exp. Biol.* **202** 2303–27

[33] Tsiakmakis K and Laopoulos T 2011 An improved tracking technique for visual measurements of ionic polymer–metal composites (IPMC) actuators using Compute Unified Device Architecture (CUDA) *Meas. Sci. Technol.* **22** 114006

[34] Canny J 1986 A computational approach to edge detection *IEEE Trans. Pattern Anal.* **8** 679–98

[35] Dewar H and Graham J B 1994 Studies of tropical tuna swimming performance in a large water tunnel *J. Exp. Biol.* **192** 45–59

[36] Tytell E D and Lauder G V 2004 The hydrodynamics of eel swimming. I. Wake structure *J. Exp. Biol.* **207** 1825–41

[37] Wen L, Wang T, Wu G and Li J 2011 A novel method based on a force-feedback technique for the hydrodynamic investigation of kinematic effects on robotic fish *Proc. IEEE/RSJ Int. Conf. on Robotics and Automation (Shanghai, China, 2011)* pp 203–8

[38] Wen L, Wang T, Wu G, Liang J and Wang C 2012 Novel method for modeling and control investigation of efficient-swimming carangiform robotic fish *IEEE Trans. Indust. Electron.* **59** 3176–88

[39] Wen L, Wang T, Wu G and Liang J 2012 Hydrodynamic investigation of a self-propulsive robotic fish based on a force-feedback control method *Bioinsp. Biomim.* **7** 036012

[40] Wen L, Wang T, Wu G and Liang J 2012 Hybrid undulatory kinematics of a robotic mackerel (Scomber scombrus): theoretical modeling and experimental investigation *Sci. China Technol. Sci.* **55** 2941–52

[41] Beal D N, Hover F S, Triantafyllou M S, Liao J C and Lauder G V 2006 Passive propulsion in vortex wakes *J. Fluid Mech.* **549** 385–402

[42] Bandyopadhyay P R 2005 Trends in biorobotic autonomous undersea vehicles *IEEE J. Oceanic Eng.* **30** 109–39

[43] Tan G K, Shen G X and Huang S Q 2007 Investigation of flow mechanism of a robotic fish swimming by using flow visualization synchronized with hydrodynamic force measurement *J. Exp. Fluids* **43** 811–21

[44] Brucker C and Bleckmann H 2007 Vortex dynamics in the wake of a mechanical fish *J. Exp. Fluids* **43** 799–810

[45] Tangorra J, Anquetil P, Fofonoff T, Chen A, Del Z M and Hunter I 2007 The application of conducting polymers to a biorobotic fin propulsor *Bioinsp. Biomim.* **2** 6–17

[46] Lee S, Park H C and Kim K J 2005 Equivalent modeling for ionic polymer–metal composite actuators based on beam theories *Smart Mater. Struct.* **14** 1363–8

[47] Dogruer D, Lee J, Yim W, Kim K J and Kim D 2007 Fluid interaction of segmented ionic polymer–metal composites under water *Smart Mater. Struct.* **16** 220–6

[48] Ming A, Park S, Nagata Y and Shimojo M 2009 Development of underwater robots using piezoelectric fiber composite *Proc. IEEE Int. Conf. on Robotics and Automation (Kobe, Japan, 2009)* pp 3821–6

[49] Rossi C, Colorado J, Coral W and Barrientos A 2011 Bending continuous structures with SMAs: a novel robotic fish design *Bioinsp. Biomim.* **6** 045005

[50] Zhang Z, Philen M and Neu W 2010 A biologically inspired artificial fish using flexible matrix composite actuators: analysis and experiment *Smart Mater. Struct.* **19** 094017

[51] Blake R W 2010 Special issue on the biomimetics of aquatic lift: applications for engineering *Bioinsp. Biomim.* **5** 030201

[52] Borazjani I and Sotiropoulos F 2010 On the role of form and kinematics on the hydrodynamics of self-propelled body/caudal fin swimming *J. Exp. Biol.* **213** 89–107

[53] Fish F E and Lauder G V 2006 Passive and active flow control by swimming fishes and mammals *Annu. Rev. Fluid Mech.* **38** 193–224